npj | 2D materials and applications

www.nature.com/npj2dmaterials

ARTICLE OPEN

Tailoring the dielectric screening in WS_2–graphene heterostructures

David Tebbe[1], Marc Schütte[1], Kenji Watanabe[2], Takashi Taniguchi[3], Christoph Stampfer[1,4], Bernd Beschoten[1,5] and Lutz Waldecker[1] ✉

The environment contributes to the screening of Coulomb interactions in two-dimensional semiconductors. This can potentially be exploited to tailor material properties as well as for sensing applications. Here, we investigate the tuning of the band gap and the exciton binding energy in the two-dimensional semiconductor WS_2 via the external dielectric screening. Embedding WS_2 in van der Waals heterostructures with graphene and hBN spacers of thicknesses between one and 16 atomic layers, we experimentally determine both energies as a function of the WS_2-to-graphene interlayer distance and the charge carrier density in graphene. We find that the modification to the band gap as well as the exciton binding energy are well described by a one-over-distance dependence, with a significant effect remaining at several nanometers distance, at which the two layers are electrically well isolated. This observation is explained by a screening arising from an image charge induced by the graphene layer. Furthermore, we find that the effectiveness of graphene in screening Coulomb interactions in nearby WS_2 depends on its doping level and can therefore be controlled via the electric field effect. We determine that, at room temperature, it is modified by approximately 20% for charge carrier densities of $2 \times 10^{12}\,\mathrm{cm}^{-2}$.

npj 2D Materials and Applications (2023)7:29 ; https://doi.org/10.1038/s41699-023-00394-0

INTRODUCTION

Embedding two-dimensional (2D) semiconductors, such as transition metal dichalcogenides (TMDs), into van der Waals heterostructures offers a wide variety of opportunities for tuning material properties and creating functionalities. These range from the improvement of the homogeneity of light emission[1–3], the creation of vertical and lateral heterojunctions[4–7], to the emergence of hybridized electronic states[8] and twist-angle dependent phenomena[9,10]. Even in the absence of electronic hybridization, the intrinsic opto-electronic properties of the 2D semiconductor strongly depend on the neighboring materials. In particular, dielectric screening by the environment modifies Coulomb interactions between charge carriers in 2D semiconductors[11]. This dielectric screening manifests as a reduction of exciton binding energies compared to monolayers in vacuum[6,12] and is accompanied by a reduction of the quasiparticle band gap due to a weaker electron self-interaction[6,13–15]. Controlling the dielectric environment therefore constitutes a way of tailoring material properties, which can be exploited, e.g., to induce lateral heterojunctions in 2D semiconductors[14,16]. Importantly, it can be applied in addition to more traditional means, such as alloying, straining, or doping[17–19].

So far, modifications to the external screening have mainly been investigated using TMDs in direct contact with various substrate materials[6,16,20,21]. For real applications, however, it might be necessary to both electrically isolate the two layers as well as to obtain a more gradual control over the dielectric screening.

Electrical isolation could, for example, be achieved using thin hexagonal boron nitride (hBN) as spacer layers[22,23]. The effect of thin spacer layers on the screening has been investigated using *GW* calculations, which predict that the quasiparticle band gap of the TMD decreases with a one-over-distance dependence[24,25]. These calculations, however, have experimentally not been tested and also do not describe excitonic effects, which dominate the optical spectra of the TMDs.

Additional tunability of the screening has been suggested to be possible by changing the charge carrier density of graphene[25,26]. This effect promises an in situ way of modifying the screening and has yet to be demonstrated at room temperature[27].

Here, we provide a comprehensive picture of the dielectric screening in 2D heterostructures at room temperature using the 2D semiconductor WS_2, graphene, and thin spacer layers of hBN. We quantify the tunability of the exciton binding energy as well as the quasiparticle band gap as a function of the distance between WS_2 and graphene as well as of the charge carrier density of graphene. Our results demonstrate a wide range of tunability and will allow the design of heterostructures of 2D semiconductors with (locally) well-defined material properties.

RESULTS

Sample design and preparation

The samples studied in this work consist of monolayers of WS_2 and graphene, separated by spacers of n_{hBN} layers of hBN. These heterostructures are fully encapsulated by the thicker top and bottom layers of hBN. A sketch of the sample geometry with and without spacer layers is shown in Fig. 1a. Some of the stacks contain a graphite gate and an electrical contact to the graphene layer, which allows tuning of the charge carrier density in graphene by a voltage V_G (see Fig. 3a).

All materials were first exfoliated from bulk crystals onto Si/SiO_2 wafers. Their thicknesses are then characterized by their optical

---

[1]2nd Institute of Physics and JARA-FIT, RWTH Aachen University, 52074 Aachen, Germany. [2]Research Center for Functional Materials, National Institute for Materials Science, 1-1 Namiki, Tsukuba 305-0044, Japan. [3]International Center for Materials Nanoarchitectonics, National Institute for Materials Science, 1-1 Namiki, Tsukuba 305-0044, Japan. [4]Peter Grünberg Institute (PGI-9) Forschungszentrum Jülich, 52425 Jülich, Germany. [5]JARA-FIT Institute for Quantum Information, Forschungszentrum Jülich GmbH and RWTH Aachen University, 52074 Aachen, Germany. ✉email: waldecker@physik.rwth-aachen.de

Published in partnership with FCT NOVA with the support of E-MRS

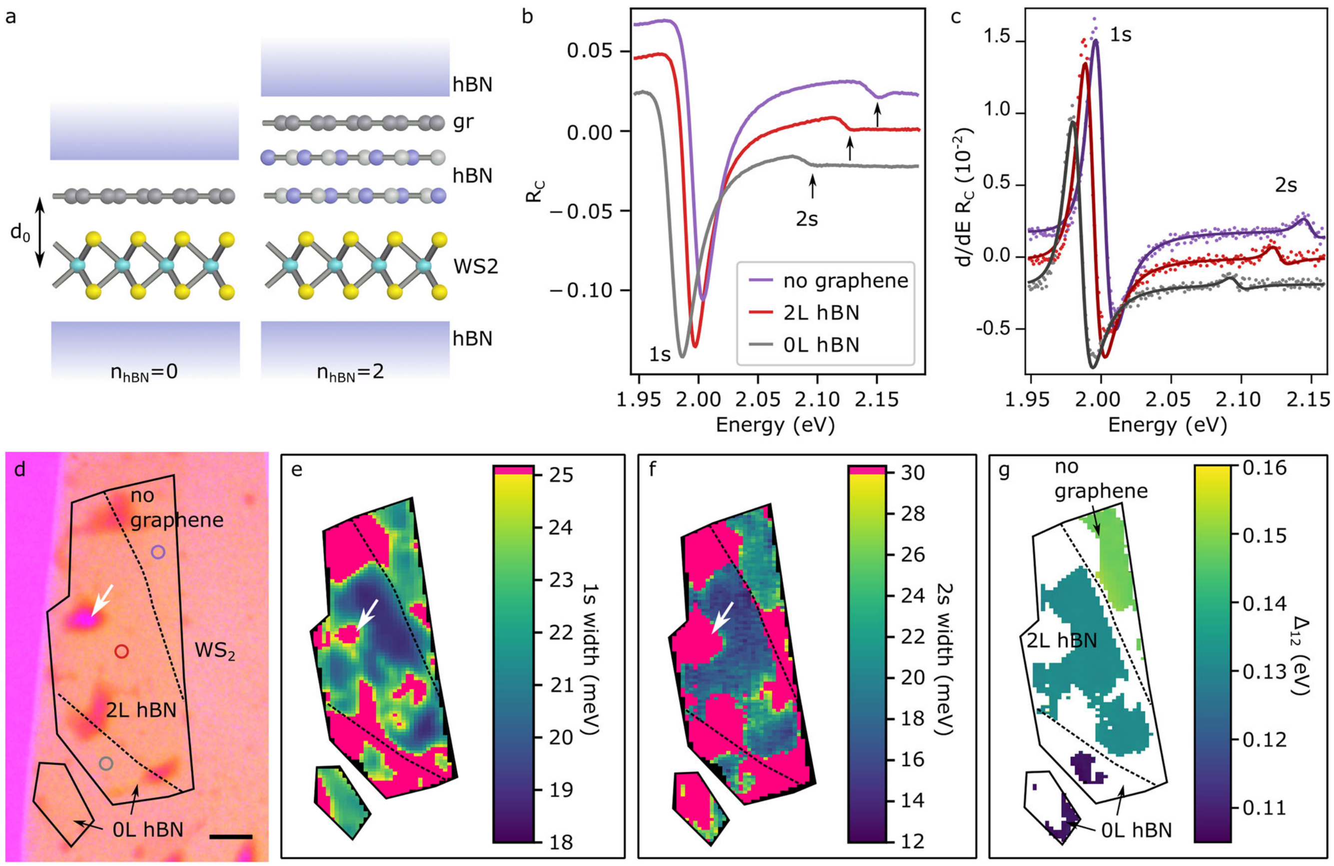

Fig. 1 Sample structure and optical measurements. **a** Sketch of the 2D heterostructure, consisting of hBN-encapsulated WS_2 and graphene monolayers, separated by n_{hBN} layers of hBN. **b** Three typical spectra taken at sample areas with 0 and 2 spacer layers as well as an area with no graphene (positions shown in (**d**)). The curves are offset vertically for clarity. **c** Derivative of the spectra (circles) shown in panel (**b**) and their respective fits (lines), offset for clarity. **d** Optical microscope image of a typical sample. The black outline denotes the area of WS_2, while the black dotted lines separate areas of different hBN spacer layer thicknesses. Scalebar: 2 µm. **e**, **f** Falsecolor maps of the 1s and 2s exciton linewidth of the sample shown in panel (**d**). **g** Map of the 1s-2s exciton level spacing Δ_{12} of the same sample. Areas of increased 1s or 2s linewidths are excluded.

contrasts toward the substrate[22], which were initially calibrated by atomic force microscopy measurements. The assembly of the stacks was performed using a polymer-based dry transfer technique[28,29] in an inert atmosphere of a glovebox (see "Methods" for details).

All heterostacks were assembled to contain areas of different thicknesses of hBN spacer layers, and a total of 10 stacks with 26 separate areas were produced in this way. Since the encapsulating hBN layers are typically more than 100 layers thick on each side, the effect of any material beyond the outer hBN on the dielectric screening is expected to be negligible[30]. Areas in which WS_2 does not directly face a graphene layer therefore serve as a reference and are treated as heterostacks with infinite layer spacing.

A heterostack containing areas of 0 and 2 hBN spacer layers as well as an area with no graphene is shown in Fig. 1d. The different areas are not discernible by their broadband optical contrast in the final stack and are thus marked in the image by dashed lines.

Distance dependence of the screening

We first determine excitonic binding energies and the quasiparticle band gaps of WS_2 in samples of different interlayer spacing. Both are obtained from whitelight reflectance contrast spectra at room temperature via the energy difference of excitonic ground (1s) and excited (2s) states. This energy is proportional to the exciton binding energy and is used since the energy of the single-particle transitions (the quasiparticle band gap) is not experimentally accessible using optical reflectance spectroscopy[6,11].

Typical reflectance contrast spectra are shown in Fig. 1b at three positions of different spacer layer thickness of the heterostack shown in Fig. 1d (exemplary spectra of every sample are shown in Supplementary Fig. 1). A small redshift of the excitonic 1s ground state feature (around 2 eV) for thinner spacer layers is visible, accompanied by a much larger redshift of the excited exciton 2s state (marked by arrows). Both indicate a simultaneous reduction of exciton binding energy and the quasiparticle band gap with reduced WS_2–graphene distance[6].

As the absolute absorption positions can vary between samples and between sample positions, e.g., due to local strain[18], we recorded reflectance spectra over the entire area of all heterostacks. The energy of the excitonic absorption features is then determined at each position by fitting the derivative of the measured spectra using a thin-film interference model[3] ("Methods" for details). Examples of the fits and the corresponding data are shown in Fig. 1c.

Figures 1e, f depict the color-coded 1s and 2s linewidth of the heterostack shown in Fig. 1d. The linewidth can be taken as an indicator for the local homogeneity of the WS_2 layer, as local strain, doping and dielectric disorder lead to line broadening[3]. We indeed find that areas of increased linewidth are usually accompanied by visible bubbles or folds in the optical micrographs; see, e.g., white arrows in Fig. 1d–f. Note that in large parts of the sample, the linewidth is found to be ≈20 meV, which is

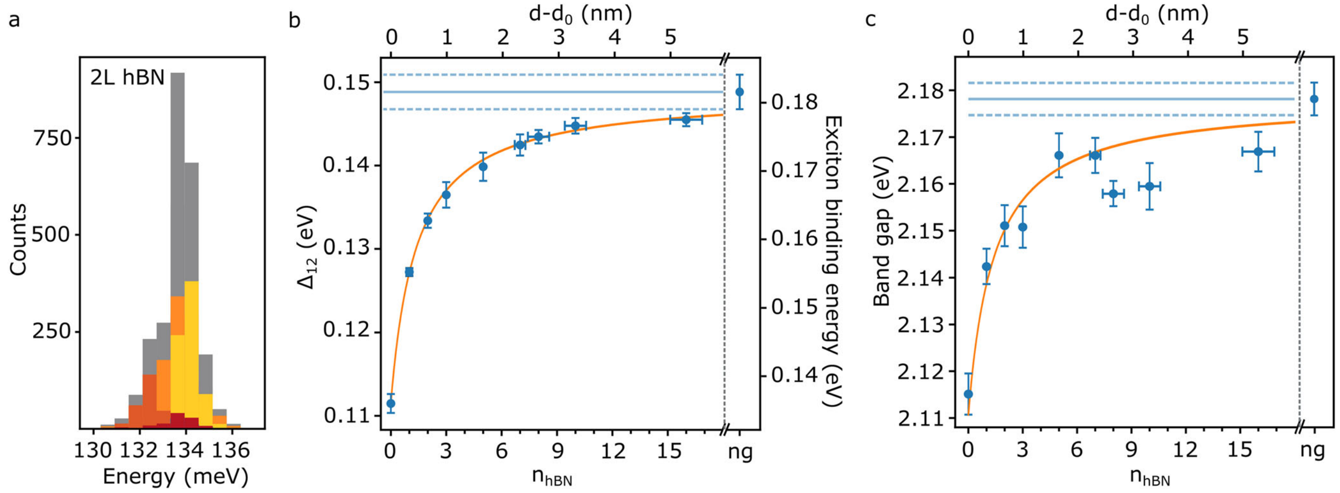

Fig. 2 Dielectric screening as a function of WS$_2$–graphene distance. a Exemplary histogram of the exciton 1s-2s energy difference for two layer thick hBN spacers and four individual samples (total: gray bars, individual samples in color). **b** Distance dependence (upper *x*-axis) of the energy separation of the excitonic 1s and 2s levels (blue points) realized by n_{hBN} hBN spacer layers (lower *x*-axis). The approximate exciton binding energy is given on the right axis (see text for details). The data point of no graphene ("ng") is equivalent to an infinite separation of WS$_2$ and graphene. The orange line is a fit to the data with a one-over-distance dependence. **c** Quasiparticle band gap as a function of hBN spacer layers and interlayer distance. The orange line depicts the fit results using a one-over-distance dependence. Datapoints and error bars in (**b**) and (**c**) are the means and standard deviations of the distribution of values of all samples.

slightly below the calculated homogeneous linewidth for WS$_2$ at room temperature[31]. We exclude areas in which the 1s (2s) linewidths exceed 25 (30) meV in the further analysis (indicated in pink in Fig. 1e, f). Figure 1g shows the 1s-2s separation, Δ_{12}, in the remaining parts of the sample. In the image, the three areas of different hBN thicknesses can clearly be distinguished.

We now analyze the distance dependence of the screening in more general terms, for which the above measurement and analysis are repeated on nine additional heterostacks. For each spacer layer thickness, we obtain a distribution of values of the 1s-2s level spacing. An example of the distribution of these values, collected on four different samples containing a two-layer hBN spacer, is shown in Fig. 2a. Typically, these distributions have widths of few meV, and sample-to-sample variations are of the same order as variations within individual samples.

The mean value of the distributions of each interlayer distance is shown in Fig. 2b, with the error bars indicating their standard deviations. To account for the smaller standard deviation of histograms to which only a single sample contributes, those errors have been multiplied by a factor of two, conservatively estimated from the sample-to-sample variations of the two-layer area. For larger hBN thicknesses, the exact determination of the hBN layer number becomes more difficult, leading to a small uncertainty in their thickness as well. The experimentally determined value for WS$_2$ with no graphene is shown as a horizontal line (dashed lines indicate the error bars).

From the 1s-2s level spacing, we calculate the exciton binding energy as $E_B \approx b \cdot \Delta_{12}$. The proportionality factor depends on the exact sample geometry and is estimated from *GW* calculations of open-faced samples to be $b = 1.2$[20] (see "Methods" for details). Note that factor b is expected to decrease with increasing screening, such that assuming a constant factor slightly underestimates the change of the binding energy[20]. The approximate exciton binding energy is nevertheless given on the right axis of Fig. 2b.

The data of Δ_{12} and the exciton binding energies show a monotonic increase with spacer layer thickness. Notably, they remain well below the values for purely hBN-encapsulated WS$_2$, even for the thickest spacers investigated here, equaling 16 layers or 5.3 nm[32].

In the simplest model, the reduction of Coulomb interactions in the 2D semiconductor arises from the electrostatic interaction of charges in the semiconductor with their image charges, which are situated at twice the distance to graphene. In this model, the screening-induced band gap modification is expected to follow a one-over-distance dependence[33,34]. It has been argued that the model will hold to a good degree for heterostructures of 2D semiconductors and graphene[25].

We thus fit the data with the relation

$$E_B = E_{B,\mathrm{ng}} - \frac{a}{2(d+d_0)}, \tag{1}$$

where $E_{B,\mathrm{ng}}$ is the exciton binding energy of WS$_2$ encapsulated in bulk hBN with no graphene, d is the hBN spacer thickness, and d_0 is the distance between the center of the TMD and the first graphene or hBN layer; see Fig. 1a, respectively (the two materials have been found to have very similar interlayer distances in heterostructures[35]). As a material-specific parameter, a is proportional to the magnitude of the screening and will be discussed in more detail in the next section. $E_{B,\mathrm{ng}}$, d_0, and a are left as free parameters in the fit, while the hBN layer thickness is given by $d = n_{\mathrm{hBN}} \cdot 3.3$ Å[32].

The fitted curve is shown as a solid orange line in Fig. 2b with the optimized parameters of $d_0 = (4.7 \pm 0.3)$ Å and $a = (126 \pm 7)$ meV Å. The obtained interlayer distance d_0 is within the error of the distance of TMDs to hBN obtained from cross-sectional TEM measurements of (5 ± 0.5) Å[36].

The distance dependence indeed well describes the exciton binding energies in the investigated range of spacer layer thicknesses, and the quality of the fit gives high confidence in the validity of the model. It thus demonstrates that it can be applied to excitons, despite them being neutral particles for which multipole screening could lead to deviations. Such deviations, however, likely only become important at interlayer distances smaller than the thickness of the TMD itself[20].

From the measurement of the 1s exciton position E_{1s} and the approximate exciton binding energy, the respective quasiparticle band gap can immediately be calculated as $E_g = E_{1s} + E_B$; see Fig. 2c. Due to small strain or doping variations, however, the absolute position of the 1s exciton fluctuates much more than the 1s-2s distance, leading to a relatively large error of those data.

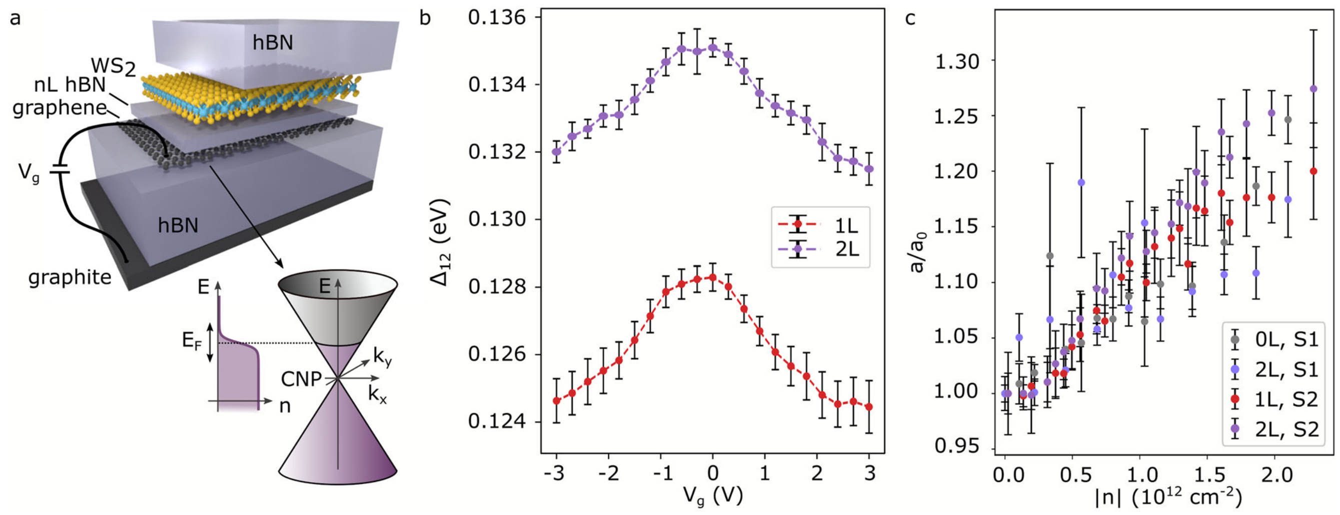

Fig. 3 **Dependence of the screening on charge carrier density in graphene.** **a** Sketch of the device geometry (top) used to tune the charge carrier density of graphene from electron ($n > 0$) to hole ($n < 0$) doping (bottom). **b** 1s-2s exciton energy difference vs. backgate voltage V_G for different hBN spacer layers. **c** Relative change of the parameter a (see Eq. (1)), proportional to the magnitude of the image charge in graphene, as a function of the absolute charge carrier density $|n|$ of graphene. S1 and S2 denote different samples. Error bars are standard deviations from analyzing several spatial positions.

Nevertheless, a one-over-distance dependence (with d_0 fixed to the previously determined value and $E_{g,\mathrm{ng}} = (2.178 \pm 0.003)$ eV) can also be used to fit the calculated quasiparticle band gap and results in a value of $a = (191 \pm 13)$ meV Å. The larger value of a for the band gap reflects the fact that its absolute change is slightly larger than the one of the exciton binding energy, as also seen in the redshift of the 1s absorption peak. This distance dependence is in qualitative agreement with theoretical calculations but of a smaller magnitude[25], which likely arises due to the absence of a top hBN layer in the calculations.

Tuning the dielectric function of graphene

We now investigate the possibility of continuously tuning the dielectric screening in the same type of heterostructures by modifying the dielectric function of graphene. This is achieved by electrostatic doping[25] via a gate voltage, which tunes the Fermi energy and therefore changes the concentration of free charge carriers in graphene (see Fig. 3a). At the same time, it modifies its dielectric function[37].

To quantify the exciton binding energy in the WS_2 layer, reflectance contrast images were taken at various gate voltages. From these spectral images, the energies of 1s and 2s excitonic states and their errors are determined in the same way as before, i.e., by analyzing and averaging every viable position in the reflectance contrast image. To verify that the applied backgate voltages do not significantly change the doping level of the TMD itself, additional photoluminescence measurements were performed, which reveal no signs of trion emission of WS_2 at any gate voltage (see Supplementary Fig. 2), possibly due to charge transfer from WS_2 to graphene[38,39]. We conclude that the doping of the TMD is negligible, and the observed modifications of the exciton binding energies result from an external change in dielectric screening.

The energy difference between 1s and 2s states, Δ_{12}, of a sample containing areas of one and two hBN spacer layers, is shown as a function of backgate voltage in Fig. 3b. For both positive and negative gate voltage polarities, the measured energy difference decreases with applied voltage. This corresponds to the Fermi energy being above and below the charge neutrality point (CNP) of the graphene layer and a population of free electrons or holes, respectively. The curve is found to be symmetric, which we ascribe to the electron–hole symmetry of graphene. The center is found to be at a voltage of approximately −0.25 V, which points to a low residual doping level of graphene. The absolute change of Δ_{12} in Fig. 3b is larger in areas of smaller interlayer distance, which is also expected from the distance dependence described by Eq. (1).

We assume that the data can be analyzed in terms of the parameter a as a function of the charge carrier density independent of the carrier type, $a = a(|n|)$. The data at each interlayer distance and each voltage are therefore scaled by $2(d + d_0)$, with $d_0 = (4.7 \pm 0.3)$ Å being the previously determined interlayer distance between WS_2 and graphene, and the factor 2 stems from the image charge being situated at twice the interlayer distance.

The relative change a/a_0, with $a_0 = a(|n| = 0)$, is shown in Fig. 3c vs. $|n|$ for all samples investigated. The charge carrier density is calculated from the backgate voltages by $n = \epsilon_0 \epsilon_r V_G / d_{\mathrm{hBN}}$ using the bottom hBN thickness d_{hBN} of the sample, measured using atomic force microscopy and the experimentally determined out-of-plane dielectric constant of hBN $\epsilon_r = 3.4 \pm 0.2$[40]. Indeed, all investigated sample areas show similar behavior, and no remaining dependence on interlayer distance is discernible, confirming that the charge carrier density of graphene only impacts the material parameter a. We find a to exhibit a relatively weak dependence on $|n|$ around charge neutrality, followed by a steeper rise, which starts to level off at higher charge carrier densities. The relatively weak dependence close to the CNP is ascribed to the thermal smearing of the Fermi energy, which leads to a finite density of electron and hole charge carriers ($|n_e| + |n_h|$) at $|n| = 0$ and stands in contrast to experiments at cryogenic temperature[27]. Away from the CNP, the dependence is expected to be nontrivial as both the dielectric function of graphene as well as the screening itself depend on both wavevector and frequency and cannot fully be described analytically[37,41]. The maximum observed modification of the parameter a is approximately 20%, which is reached at a charge carrier density slightly above $2 \times 10^{12}\,\mathrm{cm}^{-2}$. This shows that, even at room temperature, electrostatic doping of graphene allows to tune Coulomb interactions in nearby 2D semiconductors such as WS_2.

DISCUSSION

In conclusion, our experimental work quantifies the tunability of excitonic binding energies and the quasiparticle band gap due to dielectric screening in TMD–graphene heterostructures with layer-controlled hBN spacers. We find that both are described well by a one-over-distance law. The distance at which half of the maximum screening-induced change (for WS_2 in direct contact with graphene) is reached is approximately at two atomic layers of hBN. This shows that it is possible to simultaneously electrically isolate the two materials[22] while retaining a significant effect of the screening. It is important to note that, while these results have been obtained at room temperature, the same law is expected to hold at cryogenic temperatures.

We have furthermore shown that electrostatic gating of the graphene layer leads to a change of the exciton binding energies in WS_2 at various interlayer distances and have quantified the change in a single parameter. We have reached modifications of this parameter of up to 20%, limited by a finite density of free charge carriers at charge neutrality and the maximum voltages applied to the samples.

While the tuning of the exciton properties of WS_2 is substantial, we identify several avenues for increasing the absolute changes. By using spacer layers and an encapsulating material with an effective dielectric function smaller than that of hBN at frequencies in the infrared[41], both the maximum exciton binding energy as well as the absolute changes will be increased. Furthermore, the gate-induced screening effect at low densities is limited by the minimal charge carrier density of graphene due to thermal broadening. While this is straightforwardly reduced by cooling down the samples, it could also be achieved at room temperature by replacing graphene with a material possessing a small band gap.

We expect the measured distance dependence of dielectric screening to be valid for various kinds of two-dimensional bilayer structures. Such systems have recently become of interest in several contexts, such as for the investigation of interlayer excitons[4], doubly charged excitons[42], excitonic Bose–Einstein condensation[43], correlation effects[44] as well as for the investigation of light–matter interactions in TMD superstructures[45]. We have furthermore shown that electrostatically varying the charge carrier density of graphene in the vicinity of a TMD allows for a continuous and significant change in Coulomb interactions even at room temperature. Combining both approaches might lead to a novel way of studying Coulomb interactions in 2D materials showing complex interactions.

METHODS

Sample preparation

Bulk crystals were obtained from hq graphene (WS_2), NGS Naturgraphit (graphite), and NIMS (hBN). In the first step, all bulk materials were cleaved using standard tape exfoliation. The tapes were pressed onto Si/SiO_2 substrates, and suitable layers were identified optically by their color contrast to the substrate[46] (90 nm oxide for graphitic layers and thick hBN and 70 nm oxide for WS_2 and monolayer hBN). The correspondence of color contrast and thickness was initially confirmed using atomic force microscopy (for hBN and graphene) and PL spectroscopy for WS_2.

The assembly of the stacks generally follows the recipe described in ref. [29]. The top layer of hBN is picked up with a stamp made of a thin layer of polycarbonate (PC) placed on a piece of polydimethylsiloxane, which is held by a microscope cover glass. The other layers are picked up subsequently from top to bottom. The approximate temperature at the pickup is 90–110 °C. The whole stack is then released onto a substrate by heating up to 180 °C, which releases the polymer film from the PDMS. Nine out of ten samples are on Si/SiO_2 (285 nm) substrates, and one stack is on a quartz substrate. Lastly, the polycarbonate is then dissolved in chloroform, leaving the final stack on the substrate.

Reflectance contrast measurements

To record the reflectance contrast image, a tungsten whitelight source was focused onto the sample by a 100x, NA = 0.9 objective. The sample was then moved using an xy-scanning table, and the reflectance spectra were recorded at every position using a grating spectrometer. Typical integration times at each pixel are 20 s.

The reflectance contrast R_C was subsequently calculated at each pixel by $R_C = I_s/I_{ref} - 1$, where I_s is the spectrum at the pixel and I_{ref} is a reference spectrum. The reference spectrum was obtained by averaging spectra from areas next to the WS_2 sample, in which all other film thicknesses are the same. All measurements were performed at room temperature.

Fits of the data

The reflected intensity measured in the experiment is a result of the interference of light reflected at the various interfaces of the samples. Each reflection depends on the dielectric function of the materials above and below the interface. To fit the measured reflectance contrast spectra, we thus use a thin-film interference model (transfer matrix formalism implemented via the python package solcore[47]) to calculate the reflectance of the sample region and a reference region (same layer sequence without the sample). This calculation requires the dielectric function and film thickness of each layer. For hBN and graphene, as well as silicon and SiO_2, reported dielectric functions are used[48–51]. The thickness of hBN is determined from optical contrast images and atomic force microscopy measurements. The thicknesses of graphene and SiO_2 are 3.3 Å and 285 nm, respectively, and the thickness of silicon is taken to be semi-infinite as the substrate is several hundred micrometers thick.

The dielectric function of WS_2 is the quantity that is varied in the fit. It is constructed from three Lorentzian oscillators representing the A exciton 1s, 2s, and the B exciton 1s absorption features plus a constant offset $\epsilon(0)$: $\epsilon_{WS_2}(\omega) = \epsilon(0) + \sum_{j=1}^{3} \frac{f_j}{\omega_j^2 - \omega^2 - i\gamma_j\omega}$. The energies $\hbar\omega_j$, amplitudes f_j, and dampings γ_j of these Lorentzians as well as $\varepsilon(0)$ are the ten free parameters in the numerical optimization of the calculated vs. the measured reflection contrast. For better numerical stability of the fit, the derivative of the data is compared to the derivative of the model.

Estimation of exciton binding energy

The exciton energy levels in the two-dimensional hydrogen model scale like $E_B = \frac{1}{(n-0.5)^2}$. Therefore, $E_B = \frac{9}{8} \cdot \Delta_{12}$. For a material of non-negligible thickness, the electron–hole potential can be approximated by a Rytova–Keldysh potential[52]. As a result, the energy-level spacing is non-hydrogenic[11].

With increasing external screening, the field lines of electron–hole interactions are more restricted to the plane of the material. This not only decreases the binding energy but also makes it more 2D hydrogen-like. Although no analytic expressions for $b(\epsilon)$ exists, in ref. [20], the band gap, as well as 1s and 2s exciton energies, are calculated for WS_2 on a substrate of effective dielectric ϵ (and with vacuum on top). Extracting the factor $b = \frac{E_g - E_{1s}}{E_{2s} - E_{1s}}$ from ref. [20], we find it to vary between 1.35 for WS_2 on hBN to 1.2 for WS_2 on graphene. With an extra capping layer of hBN replacing the vacuum, b is expected to decrease slightly further, in particular for the less-screening case (WS_2 on hBN). Here, we take a value of $b = 1.2$, which is likely in the lower range of possible values. Note that this approximation underestimates the change of binding energy between different WS_2–graphene distances with an estimated maximum error (0 spacer layers to no graphene) in the 10% range.

DATA AVAILABILITY

The data that support the findings within this paper are available at https://doi.org/10.5281/zenodo.7802587.

Received: 2 November 2022; Accepted: 28 March 2023;

REFERENCES

1. Ajayi, O. A., Ardelean, J. V., Shepard, G. D., Wang, J. & Antony, A. Approaching the intrinsic photoluminescence linewidth in transition metal dichalcogenide monolayers. *2D Mater.* **4**, 031011 (2017).
2. Cadiz, F. et al. Excitonic linewidth approaching the homogeneous limit in MoS_2-based van der Waals heterostructures. *Phys. Rev. X* **7**, 021026 (2017).
3. Raja, A. et al. Dielectric disorder in two-dimensional materials. *Nat. Nanotechnol.* **14**, 832–837 (2019).
4. Fang, H. et al. Strong interlayer coupling in van der Waals heterostructures built from single-layer chalcogenides. *Proc. Natl Acad. Sci. USA* **111**, 6198–6202 (2014).
5. Ceballos, F., Bellus, M. Z., Chiu, H. Y. & Zhao, H. Ultrafast charge separation and indirect exciton formation in a MoS_2-$MoSe_2$ van der Waals heterostructure. *ACS Nano* **8**, 12717–12724 (2014).
6. Raja, A. et al. Coulomb engineering of the bandgap and excitons in two-dimensional materials. *Nat. Commun.* **8**, 15251 (2017).
7. Ersfeld, M. et al. Unveiling valley lifetimes of free charge carriers in monolayer WSe_2. *Nano Lett.* **20**, 3147–3154 (2020).
8. Wilson, N. R. et al. Determination of band offsets, hybridization, and exciton binding in 2D semiconductor heterostructures. *Sci. Adv.* **3**, 1601832 (2017).
9. Wu, F., Lovorn, T., Tutuc, E., Martin, I. & Macdonald, A. H. Topological insulators in twisted transition metal dichalcogenide homobilayers. *Phys. Rev. Lett.* **122**, 086402 (2019).
10. Seyler, K. L. et al. Signatures of moiré-trapped valley excitons in $MoSe_2/WSe_2$ heterobilayers. *Nature* **567**, 66–70 (2019).
11. Chernikov, A. et al. Exciton binding energy and nonhydrogenic Rydberg series in monolayer WS_2. *Phys. Rev. Lett.* **113**, 076802 (2014).
12. Stier, A. V., Wilson, N. P., Clark, G., Xu, X. & Crooker, S. A. Probing the influence of dielectric environment on excitons in monolayer WSe_2: insight from high magnetic fields. *Nano Lett.* **16**, 7054–7060 (2016).
13. Latini, S., Olsen, T. & Thygesen, K. S. Excitons in van der Waals heterostructures: the important role of dielectric screening. *Phys. Rev. B* **92**, 245123 (2015).
14. Rösner, M. et al. Two-dimensional heterojunctions from nonlocal manipulations of the interactions. *Nano Lett.* **16**, 2322–2327 (2016).
15. Park, S. et al. Direct determination of monolayer MoS_2 and WSe_2 exciton binding energies on insulating and metallic substrates. *2D Mater.* **5**, 025003 (2018).
16. Utama, M. I. B. et al. A dielectric-defined lateral heterojunction in a monolayer semiconductor. *Nat. Electron.* **2**, 60–65 (2019).
17. Li, H. et al. Growth of alloy $MoS_{2x}Se_{2(1-x)}$ nanosheets with fully tunable chemical compositions and optical properties. *J. Am. Chem. Soc.* **136**, 3756–3759 (2014).
18. Conley, H. J. et al. Bandgap engineering of strained monolayer and bilayer MoS_2. *Nano Lett.* **13**, 3626–3630 (2013).
19. Chernikov, A. et al. Electrical tuning of exciton binding energies in monolayer WS_2. *Phys. Rev. Lett.* **115**, 126802 (2015).
20. Waldecker, L. et al. Rigid band shifts in two-dimensional semiconductors through external dielectric screening. *Phys. Rev. Lett.* **123**, 206403 (2019).
21. Park, S. et al. The Schottky-Mott rule expanded for two-dimensional semiconductors: influence of substrate dielectric screening. *ACS Nano* **15**, 14794–14803 (2021).
22. Britnell, L. et al. Electron tunneling through ultrathin boron nitride crystalline barriers. *Nano Lett.* **12**, 1707 (2012).
23. Xu, W. et al. Determining the optimized interlayer separation distance in vertical stacked 2D WS_2:hBN:MoS_2 heterostructures for exciton energy transfer. *Small* **14**, 1703727 (2018).
24. Noori, K., Cheng, N. L. Q., Xuan, F. & Quek, S. Y. Dielectric screening by 2D substrates. *2D Mater.* **6**, 035036 (2019).
25. Riis-Jensen, A. C., Lu, J. & Thygesen, K. S. Electrically controlled dielectric band gap engineering in a two-dimensional semiconductor. *Phys. Rev. B* **101**, 121110 (2020).
26. Qiu, Z. et al. Giant gate-tunable bandgap renormalization and excitonic effects in a 2D semiconductor. *Sci. Adv.* **5**, 234 (2019).
27. Xu, Y. et al. Creation of moiré bands in a monolayer semiconductor by spatially periodic dielectric screening. *Nat. Mater.* **20**, 645–649 (2021).
28. Banszerus, L. et al. Ultrahigh-mobility graphene devices from chemical vapor deposition on reusable copper. *Sci. Adv.* **1**, 1500222 (2015).
29. Pizzocchero, F. et al. The hot pick-up technique for batch assembly of van der Waals heterostructures. *Nat. Commun.* **7**, 11894 (2016).
30. Winther, K. T. & Thygesen, K. S. Band structure engineering in van der Waals heterostructures via dielectric screening: the GΔW method. *2D Mater.* **4**, 025059 (2017).
31. Selig, M. et al. Excitonic linewidth and coherence lifetime in monolayer transition metal dichalcogenides. *Nat. Commun.* **7**, 13279 (2016).
32. Pease, R. S. Crystal structure of boron nitride. *Nature* **165**, 722–723 (1950).
33. Neaton, J. B., Hybertsen, M. S. & Louie, S. G. Renormalization of molecular electronic levels at metal-molecule interfaces. *Phys. Rev. Lett.* **97**, 216405 (2006).
34. Garcia-Lastra, J. M., Rostgaard, C., Rubio, A. & Thygesen, K. S. Polarization-induced renormalization of molecular levels at metallic and semiconducting surfaces. *Phys. Rev. B* **80**, 245427 (2009).
35. Haigh, S. J. et al. Cross-sectional imaging of individual layers and buried interfaces of graphene-based heterostructures and superlattices. *Nat. Mater.* **11**, 764–767 (2012).
36. Rooney, A. P. et al. Observing imperfection in atomic interfaces for van der Waals heterostructures. *Nano Lett.* **17**, 5222–5228 (2017).
37. Hwang, E. H. & Das Sarma, S. Dielectric function, screening, and plasmons in two-dimensional graphene. *Phys. Rev. B* **75**, 205418 (2007).
38. Zhu, B., Chen, X. & Cui, X. Exciton binding energy of monolayer WS_2. *Sci. Rep.* **5**, 9218 (2015).
39. Froehlicher, G., Lorchat, E. & Berciaud, S. Charge versus energy transfer in atomically thin graphene-transition metal dichalcogenide van der Waals heterostructures. *Phys. Rev. X* **8**, 011007 (2018).
40. Pierret, A. et al. Dielectric permittivity, conductivity and breakdown field of hexagonal boron nitride. *Mater. Res. Express* **9**, 065901 (2022).
41. Steinhoff, A., Wehling, T. O. & Rösner, M. Frequency-dependent substrate screening of excitons in atomically thin transition metal dichalcogenide semiconductors. *Phys. Rev. B* **98**, 045304 (2018).
42. Sun, Z. et al. Charged bosons made of fermions in bilayer structures with strong metallic screening. *Nano Lett.* **21**, 7669–7675 (2021).
43. Wang, Z. et al. Evidence of high-temperature exciton condensation in two-dimensional atomic double layers. *Nature* **574**, 76–80 (2019).
44. Ma, L. et al. Strongly correlated excitonic insulator in atomic double layers. *Nature* **598**, 585–589 (2021).
45. Kumar, P. et al. Light-matter coupling in large-area van der Waals superlattices. *Nat. Nanotechnol.* **17**, 182–189 (2022).
46. Müller, M. R. et al. Visibility of two-dimensional layered materials on various substrates. *J. Appl. Phys.* **118**, 145305 (2015).
47. Alonso-Álvarez, D. et al. Solcore: a multi-scale, Python-based library for modelling solar cells and semiconductor materials. *J. Comput. Electron.* **17**, 1099–1123 (2018).
48. Lee, S. Y., Jeong, T. Y., Jung, S. & Yee, K. J. Refractive index dispersion of hexagonal boron nitride in the visible and near-infrared. *Phys. Status Solidi B Basic Res.* **256**, 1800417 (2019).
49. Weber, J. W., Calado, V. E. & Van De Sanden, M. C. M. Optical constants of graphene measured by spectroscopic ellipsometry. *Appl. Phys. Lett.* **97**, 091904 (2010).
50. Green, M. A. & Keevers, M. J. Optical properties of intrinsic silicon at 300 K. *Prog. Photovolt. Res. Appl.* **3**, 189–192 (1995).
51. Malitson, I. H. Interspecimen comparison of the refractive index of fused silica. *J. Opt. Soc. Am.* **55**, 1205 (1965).
52. Rytova, N. S. Screened potential of a point charge in a thin film. *Vestn. Mosk. Univ. Fiz. Astron.* **3**, 30 (1967).

ACKNOWLEDGEMENTS

This project has received funding from the European Union's Horizon 2020 research and innovation programme under grant agreement No 881603 (Graphene Flagship) and by the Deutsche Forschungsgemeinschaft (DFG, German Research Foundation) under Germany's Excellence Strategy - Cluster of Excellence Matter and Light for Quantum Computing (ML4Q) EXC 2004/1 - 390534769. K.W. and T.T. acknowledge support from JSPS KAKENHI (Grant Numbers 19H05790, 20H00354, and 21H05233). L.W. acknowledges support from the Alexander von Humboldt Foundation.

AUTHOR CONTRIBUTIONS

L.W. conceived the project. K.W. and T.T. grew hBN crystals. D.T. and M.S. produced the samples and conducted the measurements. D.T., M.S., and L.W. analyzed the data, which was discussed by all authors. L.W. and D.T. wrote the manuscript with input from all authors.

FUNDING

Open Access funding enabled and organized by Projekt DEAL.

COMPETING INTERESTS

The authors declare no competing interests.

ADDITIONAL INFORMATION

Supplementary information The online version contains supplementary material available at https://doi.org/10.1038/s41699-023-00394-0.

Correspondence and requests for materials should be addressed to Lutz Waldecker.